

Article

Effects of Ag, Nd, and Yb on the Microstructures and Mechanical Properties of Mg-Zn-Ca Metallic Glasses

Zhuofan Liang^{1,2,†}, Lianzan Yang^{1,†}, Yongyan Li¹, Xi Wang^{1,*}, Chunling Qin¹,
Weimin Zhao^{1,*}, Hui Yu¹ and Zhifeng Wang^{1,2,*}

¹ School of Materials Science and Engineering, Hebei University of Technology, Tianjin 300130, China; zfliang2017mail@163.com (Z.L.); yanglianzan@163.com (L.Y.); liyongyan@126.com (Y.L.); clqin@hebut.edu.cn (C.Q.); yuhuidavid@126.com (H.Y.)

² Key Laboratory for New Type of Functional Materials in Hebei Province, Hebei University of Technology, Tianjin 300130, China

* Correspondence: xiwanghebut@163.com (X.W.); wmzhao@yahoo.com (W.Z.); zfwangmail@163.com (Z.W.); Tel.: +86-186-2930-4097 (X.W.); +86-22-6020-4477 (W.Z.); +86-22-6020-4129 (Z.W.)

† These authors contributed equally to this work.

Received: 19 September 2018; Accepted: 19 October 2018; Published: 20 October 2018



Abstract: Mg-Zn-Ca metallic glasses are regarded as promising biodegradable materials. Previous studies on this alloy system have mostly focused on the composition regions with a large critical size (D_c) for the formation of metallic glasses, while this paper investigates the composition regions with a small D_c , which has been overlooked by researchers for a long time. The effects of the addition of Ag, Nd, and Yb elements on the microstructure and mechanical properties of Mg-Zn-Ca metallic glasses were studied. It was found that the Mg-Zn-Ca metallic glass exhibits a single and uniform amorphous structure with a compressive strength of 590 MPa. After the addition of a small amount of Ag into the alloy, the amorphous matrix is retained and new precipitate phases that lead to the decrease of the compressive strength are formed. The addition of the rare earth elements Nd and Yb changes the microstructure from a single amorphous matrix to a large number of quasicrystal phases, which results in an increase in compressive strength. The compressive strength of the Mg-Zn-Ca-Yb alloy increases to 606.2 MPa due to the formation of multi-layered swirling solidified structure and a large number of small quasicrystals with high microhardness. Moreover, this study can be considered as a useful supplement to the existing studies on the Mg-Zn-Ca alloy system; it also provides new ideas for designing the microstructure and spatial structure of quasicrystal containing alloys with high performances.

Keywords: Mg-Zn-Ca; metallic glass; rare earth; mechanical property

1. Introduction

As an environmentally friendly material, magnesium alloys have the characteristics of light weight and high reserve content in the earth crust. Therefore, they have been widely used in electronic products and medical equipment [1,2]. Compared to traditional crystalline magnesium alloys, Mg-based amorphous alloys exhibit a higher compressive strength and corrosion resistance as they have a uniform structure with almost no defects such as grain boundaries and dislocations [3–6].

Mg-Zn-Ca metallic glass is a typical Mg-based amorphous alloy. It is safe and non-toxic as all of its constituent elements are essential elements in the human body. The alloy is considered to be a promising biodegradable material and has attracted significant attention worldwide [6–8]. The existing literature on this alloy system focuses on the following aspects. Firstly, some studies attempted to obtain Mg-Zn-Ca alloys with a large critical size (D_c) for the formation of metallic glass. In this way,

the application range of the alloys can be extended [9–11]. It is reported that the $Mg_{60}Zn_{35}Ca_5$ alloy presents a D_c of only 1 mm and the $Mg_{67}Zn_{28}Ca_5$ alloy has $D_c = 4$ mm [12,13]. The largest glass forming sizes are located in $Mg_{66}Zn_{30}Ca_4$ and $Mg_{67}Zn_{29}Ca_4$, with $D_c = 5$ mm [9,13,14]. Secondly, Mg-Zn-Ca metallic glasses may generate hydrogen gas when they are implanted into an animal's body. Therefore, avoiding the flow-out of hydrogen gas is indispensable for promoting the application of such alloys. Löffler et al. [8] reported that when the Zn concentration is more than 28 at %, no hydrogen generation can be detected during material degradation. That means the hydrogen gas flow-out problem can be effectively solved by modifying the original composition of the alloy. Thirdly, the corrosion resistance of Mg-Zn-Ca alloys is relatively poor. As a result, the implanted material may lose its effect before the completion of the service period due to its excessive degradation. Improving the corrosion resistance or reducing its degradation rate is therefore an important research topic. Previous studies indicate that the corrosion resistance of Mg-Zn-Ca metallic glasses can be effectively enhanced by adding Sr, Ag, and a small amount of rare earth element Y [15–17], or synthesizing a corrosion-resistant coating on the alloys [18–22]. Fourthly, Mg-Zn-Ca metallic glasses are hard and brittle, with several studies focused on improving their plasticity, which is of great significance for their practical application. Wang et al. [23] introduced a Yb element into the Mg-Zn-Ca alloy and the as-formed Mg-Zn-Ca-Yb amorphous ribbon showed excellent plasticity. Qin et al. [24] added Ag into the Mg-Zn-Ca alloy and found that the D_c is largest when the content of Ag is around 1 at %. The as-obtained Mg-Zn-Ca-Ag alloy exhibited excellent mechanical properties. Wang et al. [25] prepared Mg-Zn-Ca-Y rod by introducing a Y element into the Mg-Zn-Ca amorphous matrix. The material exhibits improved compression plasticity for the formation of endogenous dendrites as the toughness-enhancing phase.

Most of the existing works have been carried out by selecting the composition that can form metallic glass with a large D_c [26–34], while research on metallic glass with a small D_c is still rarely reported. If a fourth component is added into the aforementioned compositions, the changes in the structure of amorphous matrix and mechanical properties of the alloys are worth noting. If a rare earth element is added, whether a quasicrystal phase can be formed needs confirming. The studies on such a series of problems are still lacking. In this paper, the effects of the addition of Ag, Nd, and Yb elements on the microstructure and mechanical properties of the Mg-Zn-Ca amorphous alloys were investigated. The study would be a useful supplement to previous works and will provide important findings for further research and applications on Mg-Zn-Ca alloys.

2. Materials and Methods

2.1. Composition Design of the Experimental Alloys

Figure 1 shows the composition range for the metallic glass formation in a ternary Mg-Zn-Ca alloy system [9]. Metallic glass rods with a D_c of at least 1 mm can be formed in the yellow area. The position of the brown rhombus corresponds to the Mg-Zn-Ca metallic glass with $D_c = 2$ mm. The position of the green triangle relates to the Mg-Zn-Ca metallic glass with a D_c of 3 mm. The gray dot presents the composition of the alloy designed by this work, with a D_c between 2 mm and 3 mm. Owing to the relatively small D_c , when a bit of the fourth component is added to the alloy, the amorphous matrix may or may not be retained. A new precipitated phase may be formed in this situation. The composition selected in this work aims at the exploration of these changes in microstructures and mechanical properties before and after the addition of the fourth component. The compositions of the experimental alloys are shown in Table 1.

2.2. Material Preparation

High-purity Mg ingot (99.99 wt %), Zn ingot (99.99 wt %), Mg-30.5 wt % Ca master alloys, Ag ingot (99.99 wt %), Nd ingot (99.99 wt %), and Yb ingot (99.99 wt %) were melted in a crucible electric resistance furnace (SG₂-5-10A) under a protection of SF₆/CO₂ mixed atmosphere. The melting temperatures of Mg-Zn-Ca, Mg-Zn-Ca-Ag, Mg-Zn-Ca-Nd, and Mg-Zn-Ca-Yb alloys are 760 °C,

1000 °C, 1050 °C, and 850 °C, respectively, depending on the melting point of the fourth component. After stabilizing for 2 min, the melt was subsequently poured into a copper mold, followed by water cooling. The master alloys were remelted twice to ensure a homogenous composition. Finally, the alloys were induction melted and spray casted into the copper mold to obtain rods with a diameter of 2 mm and a length of 4 cm. The samples were further machined to a length of 4 mm (some samples were produced with a diameter of 3 mm and a length of 6 mm) for microstructural observation and compression tests.

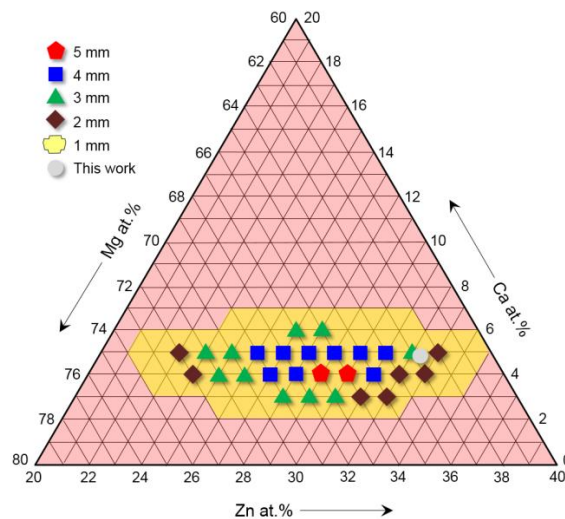


Figure 1. Composition range for the metallic glass formation in Mg-Zn-Ca ternary alloy system. Adapted with permission from Springer Nature, Copyright 2009 [9].

Table 1. The compositions of the experimental alloys (at %).

Alloy	Mg	Zn	Ca	Ag	Nd	Yb
Mg-Zn-Ca	62.9	32.3	4.8	-	-	-
Mg-Zn-Ca-Ag	63	30.2	4.5	2.3	-	-
Mg-Zn-Ca-Nd	59.8	33.1	4.7	-	2.4	-
Mg-Zn-Ca-Yb	59.3	32.4	4.8	-	-	3.5

2.3. Microstructure and Mechanical Properties

The phases were characterized via X-ray diffraction (XRD, Bruker D8) with Cu K α radiation. The microstructure of the master alloys and compositions of precipitated phase were analyzed using a scanning electron microscope (SEM, Hitachi S4800) equipped with energy-dispersive spectroscopy (EDS). The compressive tests (five samples were tested for each composition) were conducted with an UTM5105X testing machine at room temperature. The fracture morphologies of the local area were determined by SEM.

3. Results and Discussion

Figure 2 shows the XRD results of the experimental alloys. It can be seen from Figure 2a that the XRD curve of Mg_{62.9}Zn_{32.3}Ca_{4.8} alloy exhibits typical broad (halo) peak [24], demonstrating that the alloy obtained by spray casting is indeed an amorphous alloy. When a small amount of Ag is incorporated, the broad peaks of the amorphous alloy are still visible while a few sharp crystal peaks appear, which are attributed to the formation of Mg_{102.08}Zn_{39.6} phase and Ag₃Mg phase. Compared to the sample with a diameter of 2 mm, the positions of diffraction peaks slightly shifted to a larger angle (to the right) for the sample with a higher diameter of 3 mm, indicating that more Ag₃Mg phase precipitated in the matrix.

Figure 2b shows the XRD patterns of the $Mg_{62.9}Zn_{32.3}Ca_{4.8}$ alloy after introducing Nd and Yb rare earth elements. It can be seen that when rare earth elements are added, the broad peaks disappear, indicating that the amorphous matrix has changed to a crystalline structure. It means a new phase has been created. It is found that the samples with diameters of 2 mm and 3 mm were mainly composed of two phases, quasicrystal I-phase [35–37] and α -Mg phase. Compared to the sample with a diameter of 2 mm, the diffraction peaks of the sample with $D_c = 3$ mm slightly shift to a small angle (to the left). Furthermore, due to the difference in composition, the position of the diffraction peaks of the $Mg_{59.3}Zn_{32.4}Ca_{4.8}Yb_{3.5}$ alloy shifts to a smaller angle (to the left) compared to the $Mg_{59.8}Zn_{33.1}Ca_{4.7}Nd_{2.4}$ alloy.

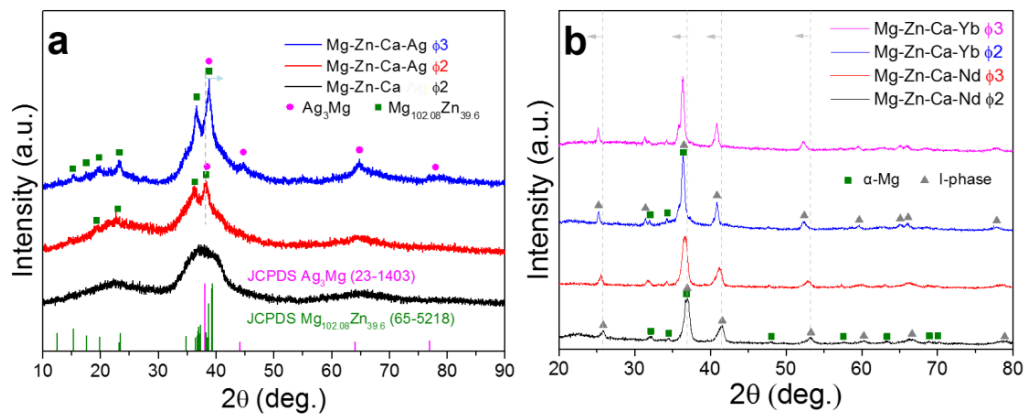


Figure 2. X-ray diffraction (XRD) patterns of (a) $Mg_{62.9}Zn_{32.3}Ca_{4.8}$ and $Mg_{63}Zn_{30.2}Ca_{4.5}Ag_{2.3}$ alloys; (b) $Mg_{59.8}Zn_{33.1}Ca_{4.7}Nd_{2.4}$ and $Mg_{59.3}Zn_{32.4}Ca_{4.8}Yb_{3.5}$ alloys.

Figure 3 shows SEM images of $Mg_{62.9}Zn_{32.3}Ca_{4.8}$ (Figure 3a) and $Mg_{63}Zn_{30.2}Ca_{4.5}Ag_{2.3}$ (Figure 3b,c) alloys. It can be seen from Figure 3a that the original Mg-Zn-Ca alloy shows a uniform microstructure with no precipitate phase. It is a typical structure of an amorphous alloy and it is consistent with the XRD data. When a small amount of Ag (2.3 at %) is added to the alloy, some precipitated phases are observed. Table 2 shows the EDS analysis of areas A, B, and C in Figure 3b. It can be seen that the composition in light gray area A is close to the $Mg_{63}Zn_{30.2}Ca_{4.5}Ag_{2.3}$ alloy, indicating an inheritance of the amorphous matrix. The Mg/Zn ratio in area B is 2.61, which is approximate to the composition of $Mg_{102.08}Zn_{39.6}$ phase. The composition of dark gray area C presents a relatively high Ag ratio, demonstrating the formation of an Ag_3Mg phase. These results are in accord with the XRD data. In this situation, a composite material containing amorphous matrix and some precipitated phases can be confirmed. Further observations show that when the sample's diameter reduces from 3 mm (Figure 3b) to 2 mm (Figure 3c), the microstructure does not change significantly, but the size of the spherical precipitated phases decreases significantly from 2~4 μm to 500~800 nm. The above result shows that after adding a small amount of Ag element to the alloy, the amorphous matrix is retained and finally an amorphous composite material containing spherical precipitated phases is formed.

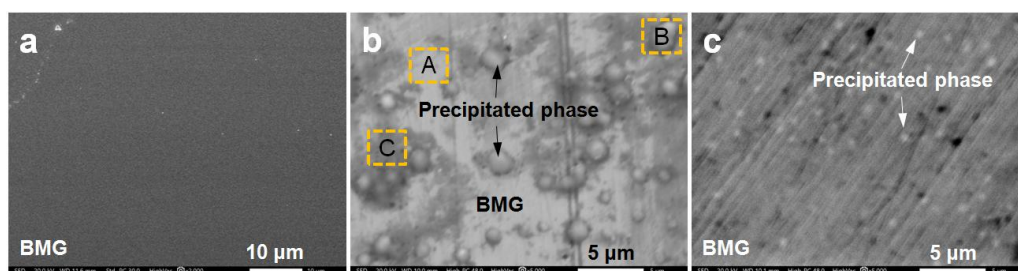


Figure 3. SEM images of experimental alloys: (a) Mg-Zn-Ca, Φ 2 mm; (b) Mg-Zn-Ca-Ag, Φ 3 mm; (c) Mg-Zn-Ca-Ag, Φ 2 mm.

Table 2. EDS analysis of areas A, B, and C in Figure 3b (at %).

Testing Area	Mg	Zn	Ca	Ag
Area A	63.2	30.3	4.3	2.2
Area B	71.1	27.2	1.1	0.6
Area C	49.3	31.1	5.5	14.1

Figure 4 shows the microstructures of the Mg-Zn-Ca alloy after the addition of Nd and Yb rare earth elements. It can be seen that, when the rare earth elements are added, the microstructures change significantly. After adding Nd, a typical quasicrystal petal phase [36] is formed in the alloy. When the sample's diameter reduces from 3 mm to 2 mm, the quasicrystal petals changes from multi-lobed to nearly spherical shape [35,37], exhibiting a rapidly decreasing petal length ranging from 5~9 μm to 1~3 μm . In addition to the quasicrystal petal phase, the primary phase of the alloy matrix is α -Mg phase and a lamellar eutectic composed of quasicrystal I phase and α -Mg phase.

As seen from Figure 4c–f, when a certain amount of rare earth element Yb is added into the Mg-Zn-Ca ternary alloy, a composite material composed of α -Mg and quasicrystal petal phase is formed. Unlike the alloy with Nd additions, no eutectic is formed when Yb is added. When the sample's diameter is 3 mm, the alloy's primary structure is α -Mg matrix and the quasicrystal petals appear as the precipitated phase. When the sample's diameter reduces to 2 mm, the quasicrystal petals are very densely distributed while the α -Mg region is greatly reduced. In this situation, the size range of the quasicrystal petal rapidly reduces from 5~7 μm (sample with $D_c = 3$ mm) to 2~3.5 μm (sample with $D_c = 2$ mm). It is further observed that the sample with $D_c = 2$ mm is rapidly cooled and forms structures with a liquid-flow swirling morphology since the molten metal rapidly fills up the mold. At the edge of the swirling region (region A), a multi-layer structure composed of small-size quasicrystal phases and α -Mg matrix is formed. In the center of the swirling region (region B), the solidification conditions are relatively uniform and the quasicrystal particles are uniformly distributed. The macroscopic morphologies and the compositions of regions A and B are different. The compositions of regions A and B based on EDS tests are shown in Table 3, in which the main difference is that the Mg content in region A is lower than that in region B. Such a multi-layer swirling structure provides us with a new idea for designing high-performance quasicrystal alloys.

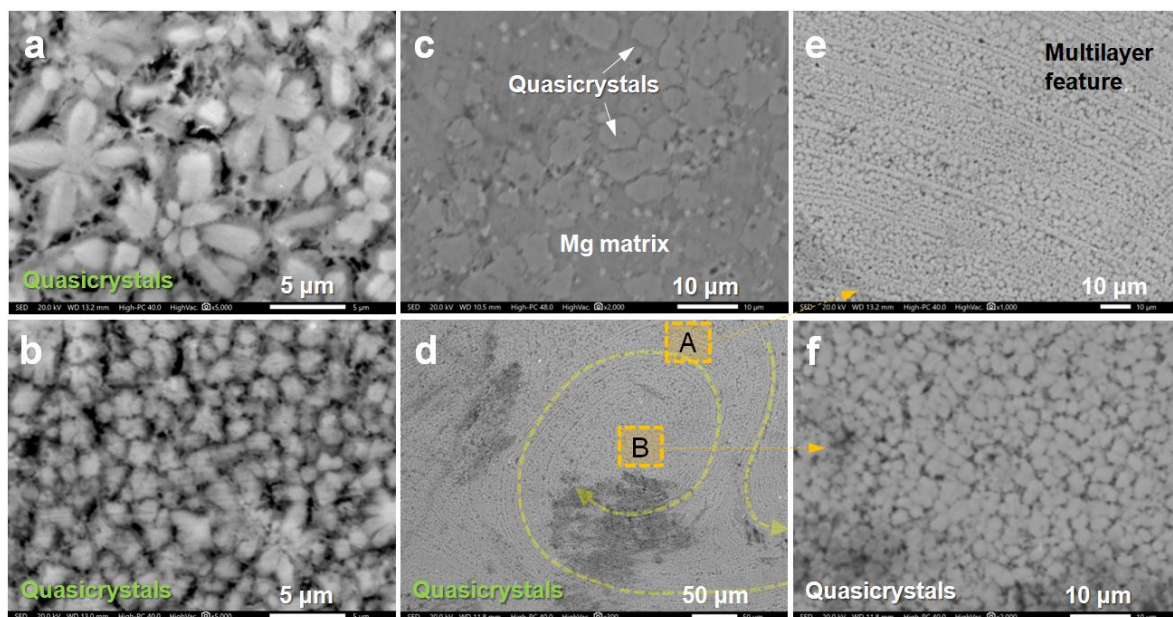


Figure 4. SEM images of experimental alloys: (a) Mg-Zn-Nd, Φ 3 mm; (b) Mg-Zn-Ca-Nd, Φ 2 mm; (c) Mg-Zn-Ca-Yb, Φ 3 mm; (d–f) Mg-Zn-Ca-Yb, Φ 2 mm.

Based on the testing results relative to Figure 4, it is found that when rare earth elements are introduced into the Mg-Zn-Ca alloy under the current experimental conditions, the amorphous structures cannot be retained and a large amount of Mg-Zn-RE quasicrystal phases forms instead. On the one hand, the rapid copper mold cooling conditions are more suitable for the nucleation process of the Mg-Zn-RE quasicrystal phases. Meanwhile, it can limit the growth of the quasicrystal phases to a certain extent, so that only moderate growth occurs. On the other hand, the rare earth element has a higher melting point. Therefore, Mg is excessively volatilized and consumed during a high-temperature smelting process. This makes the alloy composition deviate from the design point of the original Mg-Zn-Ca ternary alloy and the compositions areas with large D_c . The above reasons led to the formation of a large amount of quasicrystal phases, which replace the amorphous region as a main product.

Figure 5 and Table 4 show the measured mechanical properties of the alloys. It can be seen that the original $Mg_{62.9}Zn_{32.3}Ca_{4.8}$ amorphous alloy shows excellent compressive strength (590 MPa). When the fourth component was added to the alloy, the variations in mechanical properties can be clearly seen. After the addition of Ag element, the compressive strength reduces to 506.5 MPa. It has been reported that when 1 at % Ag is added into the $Mg_{65}Zn_{30}Ca_5$ alloy, a quaternary $Mg_{65}Zn_{30}Ca_4Ag_1$ amorphous alloy can be formed and its mechanical properties are better than those of the ternary amorphous alloy [24]. In this study, the Ag content is relatively high. Although the amorphous matrix is retained, the precipitated phases of $Mg_{102.08}Zn_{39.6}$ [38] and Ag_3Mg [39] are formed. The hardness of the two phases is lower than that of the amorphous matrix, so the alloy's compressive strength decreases. It is worth noting that the Ag_3Mg phase possesses a long period superstructure [40], which is in favor of the plasticity maintenance of the alloy. Moreover, the majority of the alloy keeps the original amorphous matrix. As a result, the plasticity of the alloy is rarely reduced after the addition of Ag. After the addition of Nd, the compressive strength decreases to 465.5 MPa, which is related to the formation of a large number of fragile lamellar eutectic. When Yb is added, the alloy's compressive strength increases to 606.2 MPa. Such enhancement of compressive strength may be related to two factors. For one thing, when a Yb element is added, a large number of small quasicrystal particles are formed in the Mg matrix. Since there is no specific slip surface in the quasicrystal system, the dislocations cannot move easily at room temperature. Therefore, these hard and brittle quasicrystal particles act as a strengthening phase and improve the alloy's strength. For another thing, a multi-layer swirling solidified structure composed of α -Mg matrix and densely-distributed small quasicrystal particles forms during the solidification process. This tough, interlaced, dense multi-layer structure leads to increasing compressive strength. In addition, the compressive strength of samples with $D_c = 3$ mm is worse than those of samples with $D_c = 2$ mm, which may be related to the larger size of precipitated phases in the 3 mm samples.

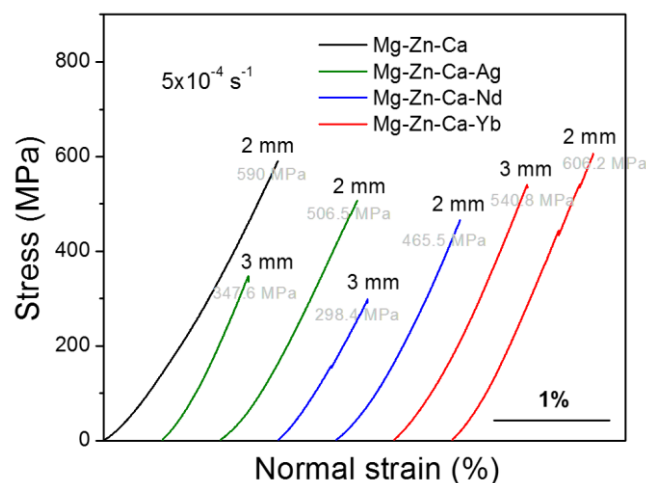


Figure 5. Compressive curves of Mg-Zn-Ca-based alloys.

Table 3. EDS analysis of area A and B in Figure 4d (at %).

Testing Area	Mg	Zn	Ca	Yb
Area A	56.9	33.8	5.4	3.9
Area B	61.7	30.7	4.4	3.2

Table 4. The comparison of the experimental alloys.

Alloy (at %)	Diameter (mm)	Compressive Strength (MPa)	Quasicrystal Phases	
			Size (μm)	Volume Fraction (%)
$\text{Mg}_{62.9}\text{Zn}_{32.3}\text{Ca}_{4.8}$	2	590 ± 5.1	-	-
	3	347.6 ± 8.2	-	-
$\text{Mg}_{63}\text{Zn}_{30.2}\text{Ca}_{4.5}\text{Ag}_{2.3}$	2	506.5 ± 7.5	-	-
	3	298.4 ± 9.3	~ 8.5	45 ± 3
$\text{Mg}_{59.8}\text{Zn}_{33.1}\text{Ca}_{4.7}\text{Nd}_{2.4}$	2	465.5 ± 6.4	~ 4.5	67 ± 4
	3	540.8 ± 5.2	~ 8	44 ± 5
$\text{Mg}_{59.3}\text{Zn}_{32.4}\text{Ca}_{4.8}\text{Yb}_{3.5}$	3	606.2 ± 4.9	~ 3.5	79 ± 3
	2	606.2 ± 4.9	~ 3.5	79 ± 3

The size and volume fraction of quasicrystal phases formed in Nd- and Yb-containing alloys can be seen from Table 4. When the rod diameter decreases from 3 mm to 2 mm, the quasicrystal size decreases and the volume fraction of quasicrystals increases obviously in both the Nd- and Yb-containing alloys. Moreover, due to a higher content of rare earth elements, the critical stable radius [37] for forming spherical quasicrystals decreases. As a result, the quasicrystal size in the Yb-containing alloy is smaller than that in the Nd-containing alloy. The amount and volume fraction of quasicrystal phases in the Yb-containing alloy are higher than in the Nd-containing alloy.

In this study, when Nd and Yb were introduced into the original alloy, the quasicrystal phase induces brittleness in the case of the Nd-containing alloy while it has a beneficial effect on the strength of the Yb-containing alloy. The microstructure of the Nd-containing alloy is mainly composed of petal-like quasicrystals with large size and lamellar eutectics. Every petal-like quasicrystal is surrounded by a lamellar eutectic network. The existence of these fragile eutectics induces obvious brittleness in the Nd-containing alloy. At the same time, the microstructure of the Yb-containing alloy is composed of quasicrystals and α -Mg. Fragile eutectics are not formed in this alloy. In particular, the multi-layer swirling structure is formed by close packing of a large number of small quasicrystals and α -Mg. Such special structure provides the possibility of improvement in the compressive strength. For another aspect, the content of rare-earth element Yb is higher than that of Nd, which induces more significant constitutional supercooling and further decreases the critical stable radius for forming spherical quasicrystals. As a result, a large amount of petal-like and spherical quasicrystals with small sizes instead of large petal-like quasicrystals are created. It was found that the smaller the quasicrystal size, the greater its microhardness [36]. So, the strengthening effect of the Yb-containing alloy is improved by these small quasicrystals.

Figure 6 shows the fracture morphologies of the samples with a diameter of 2 mm after compression testing. Figure 6a,b show the compression fracture morphologies of the $\text{Mg}_{62.9}\text{Zn}_{32.3}\text{Ca}_{4.8}$ amorphous alloy. It can be seen that the fracture surface shows a large number of herringbone fracture patterns, indicating that the overall fracture mode of the alloy is brittle. In addition, obvious vein patterns can be observed within some local areas of the fracture, showing the characteristics of local plastic fracture. These fracture pattern characteristics correspond to the good mechanical properties exhibited by the amorphous alloy. Figure 6c shows the fracture morphology of the $\text{Mg}_{63}\text{Zn}_{30.2}\text{Ca}_{4.5}\text{Ag}_{2.3}$ alloy. Both samples with diameters of 3 mm and 2 mm exhibit obvious cleavage steps, indicating that the fracture mode is a typical brittle fracture. Figure 6d and the inset show the fracture morphologies of the $\text{Mg}_{59.8}\text{Zn}_{33.1}\text{Ca}_{4.7}\text{Nd}_{2.4}$ alloy. The macroscopic fracture shows a river pattern, indicating that the fracture mode is brittle. It can be further observed from the magnified fracture structure that the quasicrystal phase and matrix in the alloy are separated during the compression process, resulting in obvious gaps and pores, which can explain the decline in

compressive strength compared to the original alloy. Figure 6e,f shows the fracture morphologies of the $\text{Mg}_{59.3}\text{Zn}_{32.4}\text{Ca}_{4.8}\text{Yb}_{3.5}$ alloy. The macroscopic fracture exhibits a river pattern, indicating that the fracture mode is also brittle. Several quasicrystal particles can be observed in the magnified fracture structure, which indicates that the crack mainly propagates along the grain boundaries at the quasicrystal edge. The dense grain distribution makes an important contribution to the higher compressive strength.

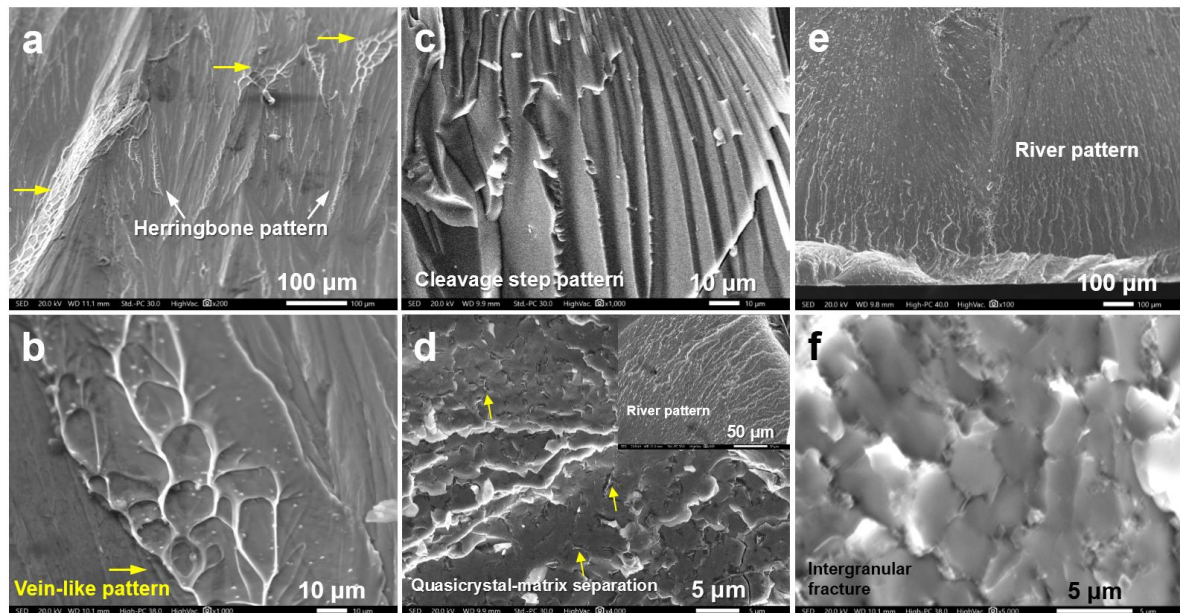


Figure 6. SEM images of the fracture morphologies of the experimental alloys: (a,b) Mg-Zn-Ca, Φ 2 mm (c) Mg-Zn-Ca-Ag, Φ 2 mm (d) Mg-Zn-Ca-Nd, Φ 2 mm (e,f) Mg-Zn-Ca-Yb, Φ 2 mm.

4. Conclusions

The present paper focused on the composition regions in a Mg-Zn-Ca alloy system with a small D_c . The effects of the addition of Ag, Nd, and Yb on the microstructure and mechanical properties of a Mg-Zn-Ca alloy were studied. It was found that the compressive strength of the Mg-Zn-Ca amorphous alloy can reach 590 MPa, showing the characteristics of overall brittle fracture (herringbone pattern) and local ductile fracture (vein pattern). After adding a small amount of Ag to the alloy, a composite material containing amorphous matrix as well as $\text{Mg}_{102.08}\text{Zn}_{39.6}$ and Ag_3Mg precipitated phases was obtained. The compressive strength reduced significantly after the addition of Ag. After the addition of Nd and Yb rare earth elements to the alloy, the microstructure with amorphous matrix is replaced by a large amount of quasicrystal phases. The Mg-Zn-Ca-Nd alloy is mainly composed of α -Mg, lamellar eutectic, and petal-shaped quasicrystal phases. The appearance of a large amount of lamellar eutectic significantly reduces the alloy's mechanical properties. However, the compressive strength of the Mg-Zn-Ca-Yb alloy increases to 606.2 MPa, which is related to its solidified dense multi-layer swirling structure and a large number of small quasicrystals with high microhardness.

Author Contributions: Z.W., X.W., and W.Z. conceived and designed the experiments; Z.L. and L.Y. performed the experiments; Z.L., L.Y., and Y.L. analyzed the data; Z.W. acquired the funding and did the project administration; Y.L., C.Q., and H.Y. contributed reagents/materials/analysis tools; X.W. and W.Z. supervised the work; Z.L. prepared the original draft; Z.W. revised the paper and created the final version.

Funding: This work was financially supported by the Natural Science Foundation of Hebei Province, China (E2015202081) and the Innovation & Entrepreneurship Training Program of Hebei University of Technology (201810080241).

Conflicts of Interest: The authors declare no conflict of interest.

References

1. Zong, X.M.; Zhang, J.S.; Liu, W.; Zhang, Y.T.; You, Z.Y.; Xu, C.X. Corrosion behaviors of long-period stacking ordered structure in Mg alloys used in biomaterials: A review. *Adv. Eng. Mater.* **2018**, *20*, 1800017. [[CrossRef](#)]
2. Xiong, H.Q.; Liang, Z.F.; Wang, Z.F.; Qin, C.L.; Zhao, W.M.; Yu, H. Mechanical properties and degradation behavior of $Mg_{(100-7x)}Zn_{6x}Y_x$ ($x = 0.2, 0.4, 0.6, 0.8$) alloys. *Metals* **2018**, *8*, 261. [[CrossRef](#)]
3. He, M.F.; Wang, H.; Zhou, K.G.; Pan, D.; Liu, F. Effects of Li addition on the corrosion behaviour and biocompatibility of Mg(Li)–Zn–Ca metallic glasses. *J. Mater. Sci.* **2018**, *53*, 9928–9942.
4. Baulin, O.; Fabrègue, D.; Kato, H.; Liens, A.; Wada, T.; Pelletier, J.M. A new, toxic element-free Mg-based metallic glass for biomedical applications. *J. Non-Cryst. Solids* **2018**, *481*, 397–402. [[CrossRef](#)]
5. Jia, H.L.; Wang, G.Y.; Chen, S.Y.; Gao, Y.F.; Li, W.D.; Liaw, P.K. Fatigue and fracture behavior of bulk metallic glasses and their composites. *Prog. Mater. Sci.* **2018**, *98*, 168–248. [[CrossRef](#)]
6. Liu, J.; Fu, Y.; Tang, Y.; Wang, X.D.; Cao, Q.P.; Zhang, D.X.; Jiang, J.Z. Thickness dependent structural evolution in Mg–Zn–Ca thin film metallic glasses. *J. Alloy. Compd.* **2018**, *742*, 524–535. [[CrossRef](#)]
7. Zheng, Y.F.; Gu, X.N.; Witte, F. Biodegradable metals. *Mater. Sci. Eng. R* **2014**, *77*, 1–34. [[CrossRef](#)]
8. Zberg, B.; Uggowitzer, P.J.; Löffler, J.F. MgZnCa glasses without clinically observable hydrogen evolution for biodegradable implants. *Nat. Mater.* **2009**, *8*, 887–891. [[CrossRef](#)] [[PubMed](#)]
9. Ma, E.; Xu, J. The glass window of opportunities. *Nat. Mater.* **2009**, *8*, 855–857. [[CrossRef](#)] [[PubMed](#)]
10. Zhang, D.; Feng, W.; Wang, X.Y.; Yang, S. Fabrication of $Mg_{65}Zn_{30}Ca_5$ amorphous coating by laser remelting. *J. Non-Cryst. Solids* **2018**, *500*, 205–209. [[CrossRef](#)]
11. Ramya, M.; Sarwat, S.G.; Udhayabanu, V.; Subramanian, S.; Raj, B.; Ravi, K.R. Role of partially amorphous structure and alloying elements on the corrosion behavior of Mg–Zn–Ca bulk metallic glass for biomedical applications. *Mater. Des.* **2015**, *86*, 829–835. [[CrossRef](#)]
12. Gu, X.; Shiflet, G.J.; Guo, F.Q.; Poon, S.J. Mg–Ca–Zn bulk metallic glasses with high strength and significant ductility. *J. Mater. Res.* **2005**, *20*, 1935–1938. [[CrossRef](#)]
13. Zhao, Y.Y.; Ma, E.; Xu, E. Reliability of compressive fracture strength of Mg–Zn–Ca bulk metallic glasses: Flaw sensitivity and Weibull statistics. *Scr. Mater.* **2008**, *58*, 496–499. [[CrossRef](#)]
14. Zhao, Y.Y.; Zhao, X. Structural relaxation and its influence on the elastic properties and notch toughness of Mg–Zn–Ca bulk metallic glass. *J. Alloys Compd.* **2012**, *515*, 154–160. [[CrossRef](#)]
15. Li, H.F.; Pang, S.J.; Liu, Y.; Sun, L.L.; Liaw, P.K.; Zhang, T. Biodegradable Mg–Zn–Ca–Sr bulk metallic glasses with enhanced corrosion performance for biomedical applications. *Mater. Des.* **2015**, *67*, 9–19. [[CrossRef](#)]
16. Li, H.F.; Pang, S.J.; Liu, Y.; Liaw, P.K.; Zhang, T. In vitro investigation of Mg–Zn–Ca–Ag bulk metallic glasses for biomedical applications. *J. Non-Crystal. Solids* **2015**, *427*, 134–138. [[CrossRef](#)]
17. Wang, J.F.; Li, Y.; Huang, S.; Wei, Y.Y.; Xi, X.F.; Cai, K.Y.; Pan, F.S. Effects of Y on the microstructure, mechanical and bio-corrosion properties of Mg–Zn–Ca bulk metallic glass. *J. Mater. Sci. Technol.* **2014**, *30*, 1255–1261. [[CrossRef](#)]
18. Tokunaga, T.; Ohno, M.; Matsuura, K. Coatings on Mg alloys and their mechanical properties: A review. *J. Mater. Sci. Technol.* **2018**, *34*, 1119–1126. [[CrossRef](#)]
19. Jiang, S.; Cai, S.; Zhang, F.Y.; Xu, P.; Ling, R.; Li, Y.; Jiang, Y.Y.; Xu, G.H. Synthesis and characterization of magnesium phytic acid/apatite composite coating on AZ31 Mg alloy by microwave assisted treatment. *Mater. Sci. Eng. C* **2018**, *91*, 218–227. [[CrossRef](#)] [[PubMed](#)]
20. Zhang, D.Y.; Ge, Y.F.; Liu, G.L.; Gao, F.; Li, P.Y. Investigation of tribological properties of micro-arc oxidation ceramic coating on Mg alloy under dry sliding condition. *Ceram. Int.* **2018**, *44*, 16164–16172. [[CrossRef](#)]
21. Zhu, H.K.; Zhao, T.; Wei, Q.P.; Liu, N.; Ma, L.; Hu, Z.Q.; Wang, Y.J.; Yu, Z.M. Corrosion resistance improvement of Mg alloy AZ31 by combining bilayer amorphous DLC:H/SiN_x film with N⁺ ions implantation. *J. Alloy. Compd.* **2018**, *762*, 171–183. [[CrossRef](#)]
22. Wang, X.; Li, L.X.; Xie, Z.H.; Yu, G. Duplex coating combining layered double hydroxide and 8-quinolinol layers on Mg alloy for corrosion protection. *Electrochim. Acta* **2018**, *283*, 1845–1857. [[CrossRef](#)]
23. Yu, H.J.; Wang, J.Q.; Shi, X.T.; Louzguine-Luzgin, D.V.; Wu, H.K.; Perepezko, J.H. Ductile biodegradable Mg-based metallic glasses with excellent biocompatibility. *Adv. Func. Mater.* **2013**, *23*, 4793–4800. [[CrossRef](#)]
24. Qin, F.X.; Xie, G.Q.; Dan, Z.H.; Zhu, S.L.; Seki, I. Corrosion behavior and mechanical properties of Mg–Zn–Ca amorphous alloys. *Intermetallics* **2013**, *42*, 9–13. [[CrossRef](#)]

25. Wang, J.F.; Wei, Y.Y.; Guo, S.F.; Huang, S.; Zhou, X.E.; Pan, F.S. The Y-doped MgZnCa alloys with ultrahigh specific strength and good corrosion resistance in simulated body fluid. *Mater. Lett.* **2012**, *81*, 112–114. [[CrossRef](#)]
26. Chen, S.S.; Tu, J.X.; Hu, Q.; Xiong, X.B.; Wu, J.J.; Zou, J.Z.; Zeng, X.R. Corrosion resistance and in vitro bioactivity of Si-containing coating prepared on a biodegradable Mg-Zn-Ca bulk metallic glass by micro-arc oxidation. *J. Non-Cryst. Solids* **2017**, *456*, 125–131. [[CrossRef](#)]
27. Monfared, A.; Ghaee, A.; Ebrahimi-Barough, S. Preparation and characterization of crystallized and relaxed amorphous Mg-Zn-Ca alloy ribbons for nerve regeneration application. *J. Non-Cryst. Solids* **2018**, *489*, 71–76. [[CrossRef](#)]
28. Matias, T.B.; Roche, V.; Nogueira, R.P.; Asato, G.H.; Kiminami, C.S.; Bolfarini, C.; Botta, W.J.; Jorge, A.M., Jr. Mg-Zn-Ca amorphous alloys for application as temporary implant: Effect of Zn content on the mechanical and corrosion properties. *Mater. Des.* **2016**, *110*, 188–195. [[CrossRef](#)]
29. Wong, P.C.; Tsai, P.H.; Li, T.H.; Cheng, C.K.; Jang, J.S.C.; Huang, J.C. Degradation behavior and mechanical strength of Mg-Zn-Ca bulk metallic glass composites with Ti particles as biodegradable materials. *J. Alloys Compd.* **2017**, *699*, 914–920. [[CrossRef](#)]
30. Nowosielski, R.; Cesarz-Andraczke, K. Impact of Zn and Ca on dissolution rate, mechanical properties and GFA of resorbable Mg-Zn-Ca metallic glasses. *Arch. Civ. Mech. Eng.* **2018**, *18*, 1–11. [[CrossRef](#)]
31. Wong, P.C.; Lee, T.H.; Tsai, P.H.; Cheng, C.K.; Li, C.; Jang, J.S.C.; Huang, J.C. Enhanced mechanical properties of MgZnCa bulk metallic glass composites with Ti-particle dispersion. *Metals* **2016**, *6*, 116. [[CrossRef](#)]
32. Qin, F.X.; Ji, C.; Dan, Z.H.; Xie, G.Q.; Wang, H.; Yamaura, S.I.; Niinomi, M.; Li, Y.D. Corrosion behavior of MgZnCa bulk amorphous alloys fabricated by spark plasma sintering. *Acta Metall. Sin.* **2016**, *29*, 793–799. [[CrossRef](#)]
33. Ramya, M.; Sarwat, S.G.; Udhayabanu, V.; Raj, B.; Ravi, K.R. Exploring Mg-Zn-Ca-based bulk metallic glasses for biomedical applications based on thermodynamic approach. *Metall. Mat. Trans. A* **2015**, *46*, 5962–5971. [[CrossRef](#)]
34. Wang, J.L.; Wan, Y.; Ma, Z.J.; Guo, Y.C.; Yang, Z.; Wang, P.; Li, J.P. Glass-forming ability and corrosion performance of Mn-doped Mg-Zn-Ca amorphous alloys for biomedical applications. *Rare Met.* **2018**, *37*, 579–586. [[CrossRef](#)]
35. Wang, Z.F.; Zhao, W.M.; Qin, C.L.; Cui, Y.; Fan, S.L.; Jia, J.Q. Direct preparation of nano-quasicrystals via a water-cooled wedge-shaped copper mould. *J. Nanomater.* **2012**, *2012*, 708240. [[CrossRef](#)]
36. Wang, Z.F.; Zhao, W.M.; Li, H.P.; Ding, J.; Li, Y.Y.; Liang, C.Y. Effect of titanium, antimony, cerium and carbon nanotubes on the morphology and microhardness of Mg-based icosahedral quasicrystal phase. *J. Mater. Sci. Technol.* **2010**, *26*, 27–32. [[CrossRef](#)]
37. Wang, Z.F.; Zhao, W.M.; Hur, B.Y.; Huang, C.Y.; Yu, C.Q. Effects of the fourth component and undercooling on morphology of primary Mg-Zn-Y icosahedral quasicrystal phase under normal casting conditions. *China Foundry* **2009**, *6*, 293–299.
38. Manne, B.; Bontha, S.; Ramesh, M.R.; Krishna, M.; Balla, V.K. Solid state amorphization of Mg-Zn-Ca system via mechanical alloying and characterization. *Adv. Powder Technol.* **2017**, *28*, 223–229. [[CrossRef](#)]
39. Dai, C.; Forbes, S. On the phase transformation of Ag-41.53Mg (at.%)—An in situ XRD study. *Vacuum* **2014**, *109*, 124–126. [[CrossRef](#)]
40. Kulik, J.; Takeda, S.; de Fontaine, D. Long period superstructures in Ag₃Mg. *Acta Metall.* **1987**, *35*, 1137–1147. [[CrossRef](#)]

